University of South Carolina
Scholar Commons

Faculty Publications | Chemical Engineering, Department of

1997

Mathematical Modeling of Proton-Exchange-Membrane Fuel-Cell Stacks

Dhanwa Thirumalai

Ralph E. White
University of South Carolina - Columbia, white@cec.sc.edu

Follow this and additional works at: https://scholarcommons.sc.edu/eche_facpub

 Part of the Other Chemical Engineering Commons

Publication Info

Published in *Journal of the Electrochemical Society*, Volume 144, Issue 5, 1997, pages 1717-1723.
© The Electrochemical Society, Inc. 1997. All rights reserved. Except as provided under U.S. copyright law, this work may not be reproduced, resold, distributed, or modified without the express permission of The Electrochemical Society (ECS). The archival version of this work was published in
Thirumalai, D., & White, R.E. (1997). Mathematical Modeling of Proton-Exchange-Membrane Fuel Cell Stacks. *Journal of the Electrochemical Society*, *144*(5) 1717-1723.
Publisher's Version: http://dx.doi.org/10.1149/1.1837667

This Article is brought to you by the Chemical Engineering, Department of at Scholar Commons. It has been accepted for inclusion in Faculty Publications by an authorized administrator of Scholar Commons. For more information, please contact digres@mailbox.sc.edu.

Symposium on Electrochemical Microfabrication, M. Datta, K. Sheppard, and D. Snyder, Editors, PV 92-3, pp. 7-19, The Electrochemical Society Proceedings Series, Pennington, NJ (1992).
4. J. N. Agar and T. P. Hoar, *Discuss. Farad. Soc.*, **1**, 158 (1947); T. P. Hoar and J. N. Agar, *ibid.*, **1**, 162 (1947).
5. C. Wagner, *This Journal*, **98**, 116 (1951).
6. B. Sapoval, in *Fractals and Disordered Systems*, A. Bunde and S. Havlin, Editors, pp. 232-261, Springer-Verlag, Heidelberg (1996) and references therein.
7. B. Sapoval, R. Gutfraind, P. Meakin, M. Keddam, and H. Takenouti, *Phys. Rev. E*, **48**, 3333 (1993).
8. H. Ruiz-Estrada, R. Blender, and W. Dieterich, *J. Phys: Condens. Matter.*, **6**, 10509 (1994).
9. T. Pajkossy, *Heterogeneous Chem. Rev.* **2**, 143 (1995) and references therein.
10. M. Leibig and T. C. Halsey, *Electrochim. Acta*, **38**, 1985 (1993) and references therein.
11. B. Sapoval, *Phys. Rev. Lett.*, **73**, 3314 (1994).
12. B. Sapoval, *Pour la Sci.*, **128**, 30 (1994)
13. M. Keddam and H Takenouti, *Electrochim. Acta*, **33**, 445 (1988), and Extended Abstract d2, 1183 of 40th I.S.E. Meeting, Kyoto (1989).
14. I. Nagatsugawa, D. I. Piron, and J. Bures, *Can. J. Chem. Eng.*, **69**, 1408 (1991).
15. R. H. Cork, D. C. Pritchard, and W. Y. Tam, *Phys. Rev. A*, **44**, 6940 (1991)
16. R. N. O'Brien and P. M. Saville, *This Journal*, **140**, 122 (1993).
17. D. P. Barkey, D. Watt, Z. Liu, and S. Raber, *ibid.*, **141**, 1206 (1994).
18. A. Kuhn, Ph.D. Thesis, Université de Bordeaux (1994).
19. K. A. Linehan and J. R. de Bruyn, *Can. J. Phys.*, To be published.
20. M. Rosso, J.-N. Chazalviel, V. Fleury, and E. Chassaing, *Electrochim. Acta*, **39**, 507 (1994).
21. Z. Whang and D. Scherson, *This Journal*, **142**, 4225 (1995).
22. E. Chassaing, M. Rosso, B. Sapoval, and J.-N. Chazalviel, *Electrochim. Acta*, **38**, 1941 (1993).
23. R. Gutfraind and B. Sapoval, *J. Phys. I France.*, **3**, 1801 (1993).
24. J. A. Klingert, S. Lynn, and C. W. Tobias, *Electrochim. Acta*, **9**, 297 (1964).
25. B. Sapoval and R. Gutfraind, in *Surface Disordering, Growth, Roughening and Phase Transitions* R. Julien, J. Kertesz, P. Meakin, and D. Wolf, Editors, p. 285, Nova Sci. Pub. (1993).
26. R. Cabán and T. W. Chapman, *This Journal*, **124**, 1371 (1977).

Mathematical Modeling of Proton-Exchange-Membrane Fuel-Cell Stacks

Dhanwa Thirumalai and Ralph E. White*

Department of Chemical Engineering, University of South Carolina, Columbia, South Carolina 29208, USA

ABSTRACT

A mathematical framework for the design of proton exchange membrane fuel-cell stacks has been established. Sensitivity analysis on the steady-state model of a single fuel cell identified the inlet gas flow rates, the operating pressure, and the temperatures as the important operating parameters. A performance model of a flow field is developed to describe the flow of the reactant gases across a single cell. The reactant flow in the stack manifold is modeled to provide an engineering estimate of the variations in gas flow to the individual fuel cells in the stack. The single-cell model is integrated with the performance model of the flow field and the stack-gas manifold to predict the operational characteristics of the fuel-cell stack.

Introduction

The performance of PEM fuel cells has been modeled by a number of investigators with varying level of detail.[1-4] The fuel-cell model of Fuller and Newman[2] based on concentrated solution theory presents significant memory and computational overheads when modeling a fuel cell stack that typically consists of a large number of cells. In contrast the model of Nguyen and White[1] provides a reliable estimate of the cell voltage in the range of low to moderately high current densities at a substantially lower cost. Hence the model of Nguyen and White[1] is used to describe the performance of the fuel cell in a stack. The present work aids in the design of fuel-cell stacks by modeling the effect of the operating parameters, the flow-field design, and the gas manifold geometry on the performance of the fuel-cell stack.

A schematic diagram of the fuel-cell modeled is given in Fig. 1. In a typical stack the individual cells are connected electrically in series, and the reactant gases are supplied in parallel through a manifold. Thus the design of the gas manifold influences the distribution of gas to individual cells across the stack. Furthermore, the flow-field design determines the flow characteristics across a single fuel cell. Thus the operation of a fuel-cell stack depends on the electrochemical performance of the membrane electrode assembly (MEA), gas flow across the flow field of a single cell, gas manifolding, and stack design.

Sensitivity Analysis on Single-Cell Model

A schematic diagram of a hydrogen-oxygen PEM fuel cell is shown in Fig. 2. The equations governing the steady-state performance of a single fuel cell are given by Nguyen and White.[1] The model equations are solved for

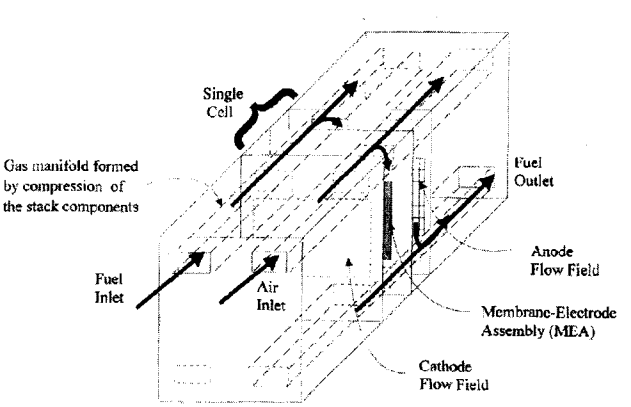

Fig. 1. Schematic diagram of the PEM fuel-cell stack, Z-manifold design.

* Electrochemical Society Active Member.

Downloaded on 2014-10-20 to IP 129.252.69.176 address. Redistribution subject to ECS terms of use (see ecsdl.org/site/terms_use) unless CC License in place (see abstract).

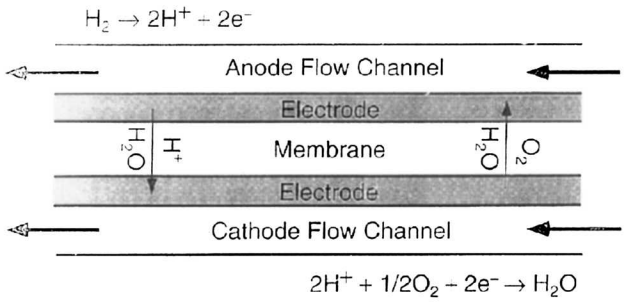

Fig. 2. Schematic diagram of the single fuel cell.

both constant-current and constant voltage operation using the software DDASAC.[5] Sensitivity analysis on the model parameters and operating conditions can be easily performed using the software. The individual cells are connected electrically in series, and hence the fuel cells will operate under constant-current conditions within the stack. For the constant-current case, the integral constraint on the local current density

$$I_{avg} = \frac{1}{L}\int_0^L I(x)dx \qquad [1]$$

is satisfied by a Newton-Raphson-type iteration for the cell voltage where V_{cell}^N is the Nth iterate of the cell voltage

$$V_{cell}^{N+1} = V_{cell}^N - \frac{I_{avg}L}{\int_0^L \frac{dI(x)}{dV_{cell}^N}dx} \qquad [2]$$

The derivative $dI(x)/dV_{cell}$ is obtained by treating V_{cell} as a sensitivity parameter and integrating the pertinent sensitivity equation across the length of the cell. This method of solution of the model equations for the constant-current case significantly increases the efficiency of computation compared to calculation of the derivative with perturbation technique.[1]

The fuel-cell model parameters and the base-case operating conditions are given in Table I. The variation of the cell voltage with current density for operation with saturated air (air contacted with water at the cell operating condition) and dry oxygen are given in Fig. 3. The effect of reactant utilization on the cell voltage at the base-case current density of 0.6 A/cm^2 is given in Fig. 4. The graphs are obtained by holding one of the reactant gases at its

Table I. Base-case model parameters and operating conditions for the simulation and sensitivity analysis of the single fuel cell. [a]

Model parameters	
Heat-transfer coefficient, U	0.0025 W/cm^2 K
Condensation rate constant k_c	1.0 s^{-1}
Membrane dry density, ρ_m	2.0 g/cm^3
Membrane dry equivalent weight, Mm	1100 g/mol
Membrane thickness, t_m	0.01275 cm
Fuel-cell open-circuit voltage V_{oc}	1.1 V
O_2 exchange current density, I_{O_2}	0.01 A/cm^2
Water diffusion coefficient parameter, D_o	5.5×10^{-7} cm^2/s
Operating conditions	
Operating current density I_{avg}	0.6 A/cm^2
Operating pressure, P	2 atm
Anode and cathode reactant inlet temperature, T_a, T_c	90°C
Temperature of the solid phase, T_s	90°C
Hydrogen utilization U_{H_2}	60%
Oxygen utilization, U_{O_2}	50%
Reactants	
Anode	H_2, H_2O
Cathode	Air, H_2O
Anode and cathode reactant inlet relative humidity	1.0

[a] Please see Ref. 1 for the model equations and the symbol definitions used in this table.

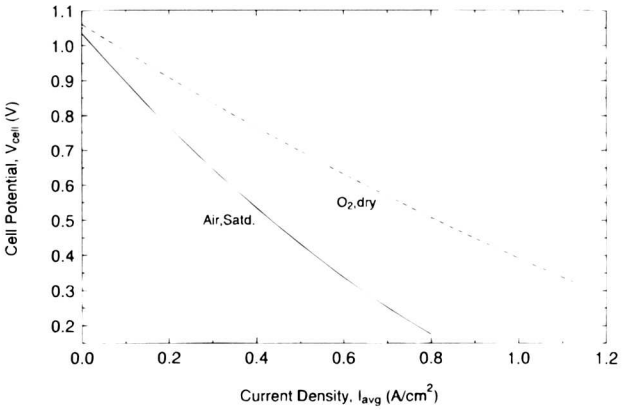

Fig. 3. Variation of cell voltage with operating current density of a fuel cell.

base-case utilization and varying the other. Utilization of species i is defined as

$$U_i = \frac{\text{consumption of species i}}{\text{moles of i in}} = \frac{\text{moles of i in} - \text{moles of i out}}{\text{moles of i in}} \qquad [3]$$

At constant current density, the consumption of species i is constant. Hence the utilization varies inversely with the inlet flow rate of the gas (*i.e.*, moles of species i in). Thus it can be inferred from Fig. 4, that as the hydrogen flow rate decreases (the H_2 utilization increases) the cell voltage drops at about 65% utilization for the specific MEA considered here. The opposite effect occurs with an increase in oxygen utilization. As the utilization of oxygen is decreased (the inlet flow rate of air is increased), the evaporative loss of water from the membrane is increased, with a consequent decrease in the membrane conductivity. The model predictions of the cell voltage variation with current density are nearly the same for operation with dry and humidified oxygen. This is because the evaporative water loss from the membrane is lower in the case of oxygen since at moderate gas utilizations the outlet gas flow rate is much lower compared to that when air is used as the cathode gas. It should be emphasized that the above effects are the predictions of the steady-state model. Hence the membrane-water equilibrium and the associated dynamics fix the time frame over which these effects are observable in practice.

A sensitivity analysis on the cell voltage of a single fuel cell under galvanostatic operation at the base-case conditions was performed using the software DDASAC. The effects of both the operating conditions and the trans-

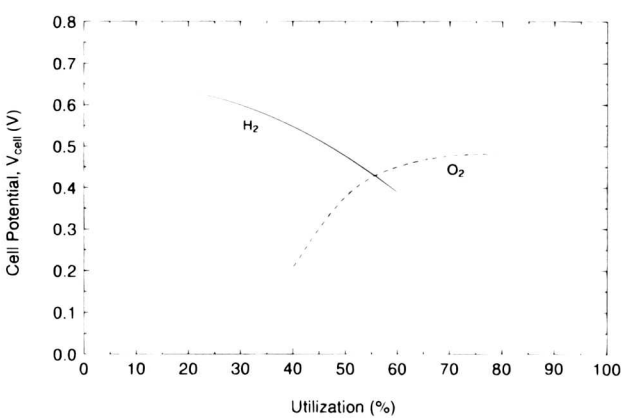

Fig. 4. Effect of reactant utilization on the cell voltage of a fuel cell.

Downloaded on 2014-10-20 to IP 129.252.69.176 address. Redistribution subject to ECS terms of use (see ecsdl.org/site/terms_use) unless CC License in place (see abstract).

port and kinetic parameters are given in Fig. 5 and 6, respectively.

The sensitivity parameter S_p^V is defined as

$$S_p^V = p\frac{dV}{dp} \quad [4]$$

where p is the value of the parameter and dV/dp is the derivative of the cell voltage with respect to the parameter p.

It can be seen from the sensitivity predictions (Fig. 5) that an increase in the utilization of hydrogen has an adverse impact on the cell voltage, especially for operation with saturated air as the oxidizer. Also, the anode relative humidity and the pressure also have a large effect on system performance. The results of the sensitivity analysis and the effect of gas utilization (*i.e.*, the inlet gas flow rates) (Fig. 4) lead us to believe that the nonuniformity in the reactant gas flow into individual cells across the stack will result in a decrease in the operational efficiency of the stack.

Results of the sensitivity analysis of the transport and kinetic parameters on the cell voltage at galvanostatic conditions are given in Fig. 6. It is seen that the sensitivity of the cell voltage with respect to the cell operating conditions is higher in the case of operation with air.

Issues in Stack Design

It can be seen from Fig. 4 and 5 that the cell voltage at constant current is a function of the inlet gas flow rates. In some severe cases, if reactant starvation occurs in a single cell due to the blockage of a flow channel due to the condensation of water, the cell fails. Since a constant current is drawn through the stack, the failed cell may start to operate as an electrolytical cell with subsequent failure of the stack. The flow through an individual cell depends on both the stack manifold design and on the specific flow pattern offered by the flow field. Thus the optimal design of the flow field and the gas manifold in the stack are coupled with the principal objective of minimizing intercell variations.

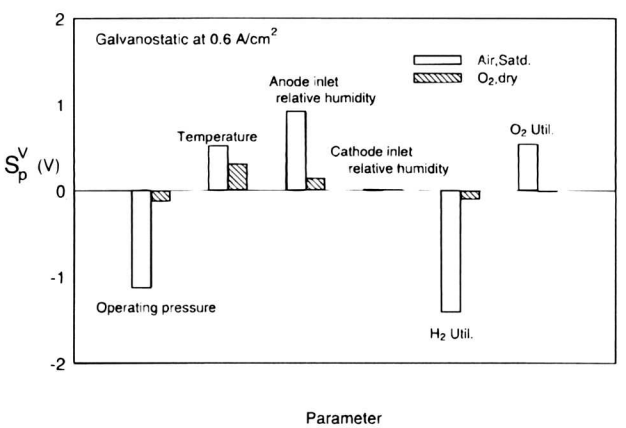

Fig. 5. Sensitivity analysis of the cell voltage of a fuel cell. Effect of operating conditions for galvanostatic operation at 0.6 A/cm².

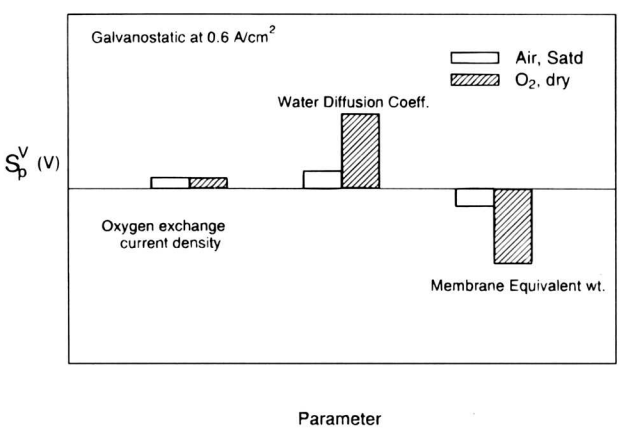

Fig. 6. Sensitivity analysis on the cell voltage of a fuel cell. Effect of transport and kinetic parameters for galvanostatic operation at 0.6 A/cm².

A schematic diagram of gas flow through the fuel-cell stack is shown in Fig. 1. A grooved carbon plate forms the flow field over which the reactant gases flow. The flow field used in the analysis is shown in Fig. 7. The flow field must provide for the effective contacting of the reactant gases with the MEA at the lowest possible pressure drop. Thus the intercell flow variations are a strong function of the flow-field design.

The flow variations within the stack can be minimized if the resistance offered by the flow field is much higher than that offered by the gas manifold. But increasing the flow field resistance increases the cost associated with the compression of the outlet gases for recirculation. Hence the cost of recompression of the outlet gas should be optimized against the cost of performance loss associated with intercell flow variations. Thus an integrated approach to the optimal design and operation of the fuel-cell stack involving the single-cell electrochemistry, flow-field design, and gas manifolding is imperative for the development of reliable fuel-cell stacks.

Fuel-cell stacks have intercell coolers (air or water cooled) to maintain the temperature of the cells within the prescribed limits. Any flow variations that arise among the individual coolers are manifested as temperature variations across the stack. Since the fuel-cell performance is a function of the operating temperature, any temperature variation introduces nonuniformity in the cell stack with the resultant loss of operating efficiency. The effect of nonuniform temperature distribution across the stack is not considered here. The present model can be easily extended to describe nonisothermal operation of the stack by modeling the coolant-flow variations similar to that of the reactant gases and following the heat transfer at each of the individual units within the stack.

Flow-Field Model

A simple model for gas flow through the flow field used in the stack (Fig. 7) is developed to describe the variation of the pressure drop with the flow rate of the gas. For simplicity the ribbed carbon plate is assumed to form a recti-

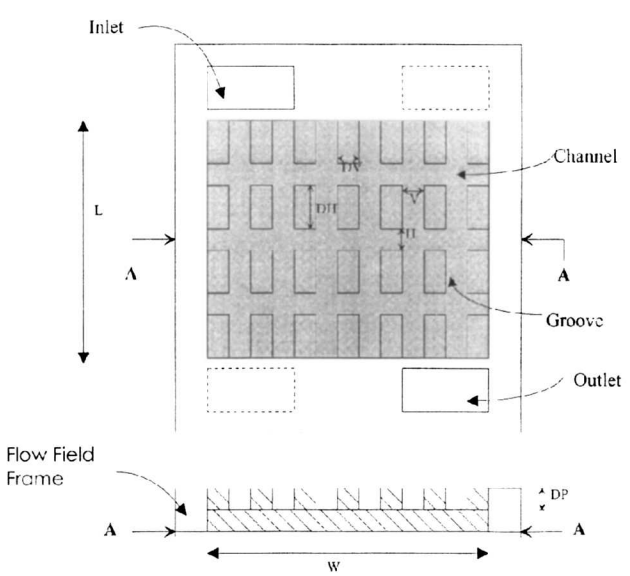

Fig. 7. Schematic diagram of the flow field used in the fuel-cell stack.

Downloaded on 2014-10-20 to IP 129.252.69.176 address. Redistribution subject to ECS terms of use (see ecsdl.org/site/terms_use) unless CC License in place (see abstract).

linear network of grooves and channels. The design parameters are the width of the channels (H) and the grooves (V) and the depth of the groove (DP). The carbon material between the grooves and channels of thicknesses DV and DH, respectively, must be kept as small as possible as they constitute a resistance to the flow. Their thicknesses are limited by the fabrication method used and the mechanical integrity of the flow fields as the stack is kept under a high cross pressure for effective electrical contact between the stack components.

The simplistic model equations for describing the performance of a flow field are derived from the laminar flow theory since the gas flow is laminar at moderately high utilization. The expansion and contraction losses occurring due to the change in flow directions are neglected, since these losses are negligible compared to the skin friction losses. The current-density distribution along the length and breadth of a single fuel cell is assumed to be uniform as a first approximation.

For laminar flow in a rectangular duct, the pressure-drop, flow-rate relationship is[6]

$$q = \frac{4ba^3}{3m} \cdot \frac{-\Delta P}{\Delta x} \cdot \left[1 - \frac{192a}{\pi^5 b} \sum_{i=1,3,5}^{\infty} \frac{\tanh\left(\frac{i\pi b}{2a}\right)}{i^5}\right] \quad [5]$$

where 2a and 2b are the width and depth of the duct, q is the flow rate of the reactant gas, and μ is the viscosity of the fluid.

Figure 8 is a representation of the flow-field pattern used for the analysis. From this figure, the mass conservation at the node (i, j) can be written as

$$-q1_{i,j} - q2_{i,j} + q1_{i+1,j} + q2_{i,j+1} + Q_{i,j} = 0 \quad [6]$$

where $Q_{i,j}$ is the volumetric consumption of the reactant at the node. Since the pressure-drop, flow rate relationship is linear, the flow conductance term can be found based on the groove and channel geometry

$$q1_{i,j} = k1_{i,j}(h_{i-1,j} - h_{i,j})$$
$$q2_{i,j} = k2_{i,j}(h_{i,j-1} - h_{i,j}) \quad [7]$$

The terms $k_{i,j}$ are found from pressure-drop flow rate relationship as

$$k_{i,j} = \frac{q_{i,j}}{-\Delta P} \quad [8]$$

where $q_{i,j}$ is represented in Fig. 8. The above equations are combined to form

$$-k1_{i,j}h_{i-1,j} - k2_{i,j}h_{i,j-1} - k1_{i+1,j}h_{i+1,j} - k2_{i,j+1}h_{i,j+1} + (k1_{i,j} + k1_{i+1,j} + k2_{i,j} + k2_{i,j+1}) \cdot h_{i,j} + Q_{i,j} = 0 \quad [9]$$

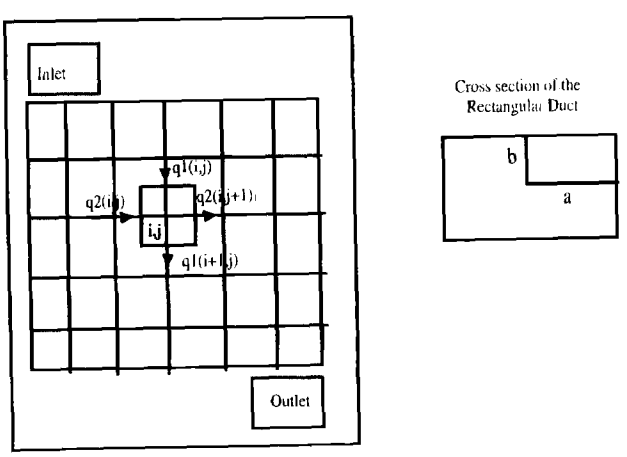

Fig 8. Geometry of the flow field used for the analysis.

which is written for each of the nodes ($nh \times nv$). The geometry of the inlet and outlet ports for the gas at a flow field is specified by the stack-gas manifold dimensions, and hence the performance of the stack and the flow field are coupled. Equations 5 to 9, with the boundary conditions determined by the flow through the cell, form a set of algebraic equations which is solved using LU factorization of the sparse matrix using IMSL routines.[7]

The effects of the flow pattern, *i.e.*, the dimensions of the grooves and channels on the pressure drop and reactant distributions can be studied. Increasing the depth of the grooves and channels, DP, results in both decreased pressure drop and a more uniform distribution. But this results in a thicker flow field and hence the power and energy density of the fuel-cell system decreases. The simulation results for the flow-field design FF1 (Fig. 9) show that the effective resistance offered to flow is a very strong function of the depth of the grooves.

The effect of consumption of the gas on the pressure drop-flow rate relationship for the flow-field design FF1 is given in Fig. 10. It is seen that the pressure drop is linearly related to the total gas flow rate and that an increase in the gas consumption leads to a decrease in the effective resistance offered by the flow field for the gas flow. Thus at constant flow rate of the gases through the cell, the operating current density affects the pressure drop across the flow field.

Gas-Manifold Model

The flow of gases in the manifold can be modeled as incompressible flow if the pressure variation is not too high. The compression and clasping of the stack components between the end plates form a gas manifold of rectangular cross section as seen in Fig. 1. The detailed analysis of the fluid flow in these manifolds involves the solution of the Navier-Stokes equation for the gas in three dimensions. The boundary conditions are specified by the relatively complicated geometry of the stack and the electrochemical reaction within the single cells. Since a commercial stack may have about 50 individual cells, solving the Navier-Stokes equation for flow throughout is not practical.

The problem can be simplified by applying a correction term for the flow split at a branch, since only an engineering estimate of the flow nonuniformity across the stack is required.[8] The anode or the cathode gas manifold can be represented by one of the schematics, U and Z manifold-

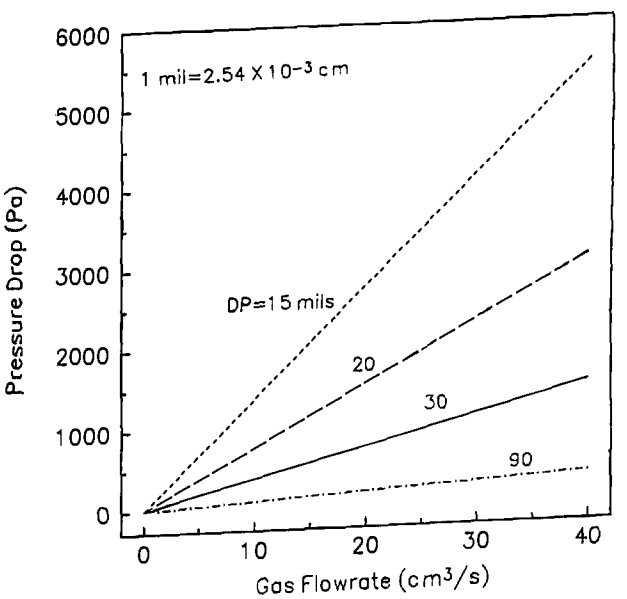

Fig. 9. Variation of pressure drop across the flow field with the gas flow rate. Effect of groove depth.

Downloaded on 2014-10-20 to IP 129.252.69.176 address. Redistribution subject to ECS terms of use (see ecsdl.org/site/terms_use) unless CC License in place (see abstract).

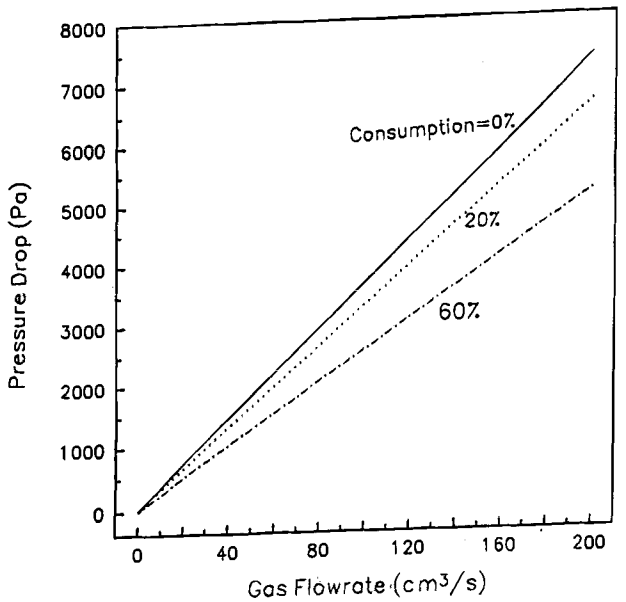

Fig. 10. Variation of pressure drop across the flow field with the gas flow rate. Effect of gas consumption.

ing, given in Fig. 11, depending on the piping connections to the stack. In fuel-cell applications, the range of the numerical values of the gas velocities and geometry favor the Z-manifold arrangement. The stack modeled is assumed to form a Z-manifold.

The principle equations governing the gas flow in a manifold, as in Fig. 11, are given below.

Momentum balance in the manifold region.—

$$p1d(n) - p1(n+1) = \frac{(a_i b_i)}{ki_m} u1(n)$$
$$p2d(n) - p2(n+1) = -s\frac{(a_o b_o)}{ko_m} u2(n) \quad [10]$$

The conductance ki_m and ko_m refer to the gas flow in the inlet and outlet manifold in the stack and are similar to that defined in Eq. 8. The parameter s takes the value +1 if the manifold is of the U-type or −1 for a Z-manifold.

Mechanical energy balance at the branch point.—

$$p1d(n) - p1(n) = k_E r[u1(n)^2 - u1(n+1)^2]$$
$$p2d(n) - p2(n) = k_D r[u2(n)^2 - u2(n+1)^2] \quad [11]$$

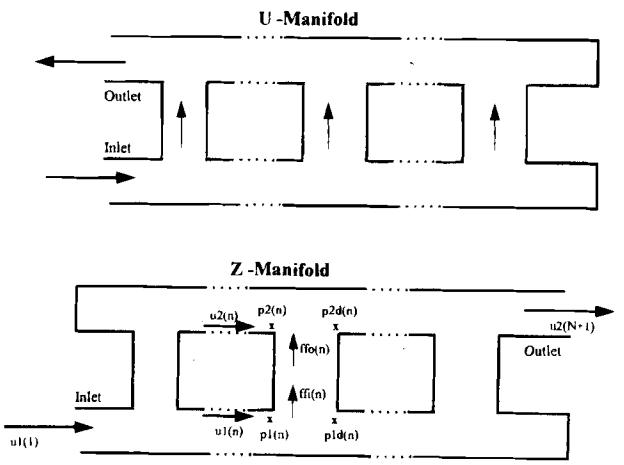

Fig. 11. Schematic diagram of the gas manifold used in the analysis.

The parameters k_E and k_D are used since the velocity of the branching fluid is not exactly normal to the direction of flow in the manifold. They can be taken as the entrance and discharge coefficients and are usually experimentally fitted for the specific fluid used.

Mass balance at the branch point.—

$$(a_i b_i)[u1(n) - u1(n+1)] = ffi(n)$$
$$(a_o b_o)[u2(n) - u2(n+1)] = sffo(n) \quad [12]$$

Here the outlet flow rate [*ffo(n)*] is related to the inlet flow rate [*ffi(n)*] by single-cell electrochemical-performance model (SCM), since the current drawn from the fuel cell affects the consumption of gas at the electrode

$$ffo(n) = SCM\{ffi(n), I_{avg}\} \quad [13]$$

where I_{avg} is the current drawn from the stack.

The flow-field model (FFM) can be used to predict the pressure drop across an individual flow field

$$\frac{1}{2}[p1(n) + p1d(n)] - \frac{1}{2}[p2(n) + p2d(n)] = \mathrm{FFM}\{ffi(n), ffo(n)\} \quad [14]$$

SCM and FFM are subroutines describing the performance of the single fuel cell and the flow field, respectively. The variables *p1d(n)* and *p2d(n)* are eliminated using Eq. 10, and Eq. 11 to 14 form a set of nonlinear algebraic equations constituting the gas-manifold model. A unique solution for the flow-distribution problem can be obtained by specifying the pressure and flow rate at the inlet and applying the boundary conditions (*i.e.*, velocities are zero at the closed ends). A modified Powell hybrid method[9] is used to solve the equations.

Fuel-Cell-Stack Operation

The fuel-cell stack can be modeled by combining the performance models of its components (*i.e.*, the single-cell model, the flow-field model, and the gas-manifold model). The component models and the parameters passed between them are given in Fig. 12. The modularity of the stack model lends itself easily to fast implementation of more sophisticated component models. The effect of various flow-field patterns on the performance of the stack can easily be tested when the flow rate pressure-drop relationship for the specific flow field is known.

The number of global iterations necessary for the convergence of the stack model and the CPU time required depends on the robustness of the component models and the implementation details of the recursive procedure used. The base-case design data are given in Table II. The solution of the fuel-cell-stack model is obtained by following the algorithm given below.

1. Fix the inlet pressure [$p1(l)$] and gas flows to the anode and cathode manifolds [$u1(l)$]. Specify the current drawn from the fuel-cell stack.

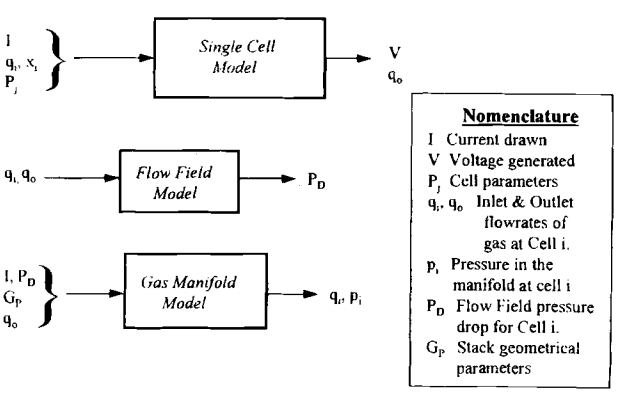

Fig. 12. Representation of the fuel-cell-stack model as an aggregate of component models.

Downloaded on 2014-10-20 to IP 129.252.69.176 address. Redistribution subject to ECS terms of use (see ecsdl.org/site/terms_use) unless CC License in place (see abstract).

Table II. Base-case design parameters and operating conditions for the fuel-cell-stack simulation.

Stack geometry	Design MN1	Design MN2
Anode		
Inlet manifold dimensions, $a_{i,A} \times b_{i,A}$	2.0 × 1.0 cm	1.8 × 0.9 cm
Outlet manifold dimensions, $a_{o,A} \times b_{o,A}$	2.0 × 1.0 cm	1.8 × 0.9 cm
Spacing between inlets	1.0 cm	1.0 cm
Cathode		
Inlet manifold dimensions, $a_{i,C} \times b_{i,C}$	1.0 × 0.5 cm	0.9 × 0.45 cm
Outlet manifold dimensions, $a_{o,C} \times b_{o,C}$	1.0 × 0.5 cm	0.9 × 0.45 cm
Spacing between inlets	1.0 cm	1.0 cm
Number of cells in the stack	5	
Electrode and flow-field width W	10.0 cm	
Electrode and flow-field length, L	10.0 cm	
Operating conditions		
Average current density, I_{avg}	0.5 A/cm^2	
Anode		
Components	H_2, H_2O	
Inlet flow rate $[a_{i,A} \times b_{i,A}) \cdot u1(1)_A]$	75.0 cm^3/s	
Inlet relative humidity	1.0	
Inlet pressure, $p1(1)_A$	2.0 atm	
Cathode		
Components	Air, H_2O	
Inlet flow rate, $(a_{i,C} \times b_{i,C}) \cdot u1(1)_c$	75.0 cm^3/s	
Inlet relative humidity	1.0	
Inlet pressure $p1(1)_c$	2.0 atm	
	Design FF1 (cm)	Design FF2 (cm)
Flow-field geometry		
Channel width, H	0.2540	0.2540
Groove width, V	0.0254	0.254
Distance between channels, DH	1.0160	1.0160
Distance between grooves, DV	0.1016	0.4064
Depth of grooves/channel, DP	0.0762	0.2

2. Solution of the gas-manifold-model equations yields the velocity $[u1(\min)]$ and $u2(n)]$ and pressure distributions $[p1(n)]$, $p1d(n)$, $p2(n)$ and $p2d(n)]$ across the stack.

3. Obtain the voltage generated by each of the individual cells $[V(n)]$ using the single-cell model. The outlet gas flow rates $[ffo(n)]$ for the single cells are also modified by the procedure.

4. Estimate the pressure drop due to the gas flow across each of the flow fields $\{[p1(n) + p1d(n)]/2 - [p2(n) + p2d(n)]/2\}$ with the modified gas inlet and outlet flow rates as predicted by the flow-field model.

5. Repeat steps 2 through 4 until convergence of the stack voltage is achieved.

The variation of the cell voltage of individual cells across the stack at the base-case operating conditions for the flow-field designs FF1 and FF2 is given in Fig. 13. It is seen that the voltage of the cells across the stack is nearly the same when the flow-field design FF1 is used. Operation of the stack with flow-field design FF2 results in a variation of the voltages generated by the cells in the stack. It is also possible to calculate the power generated in the stack.

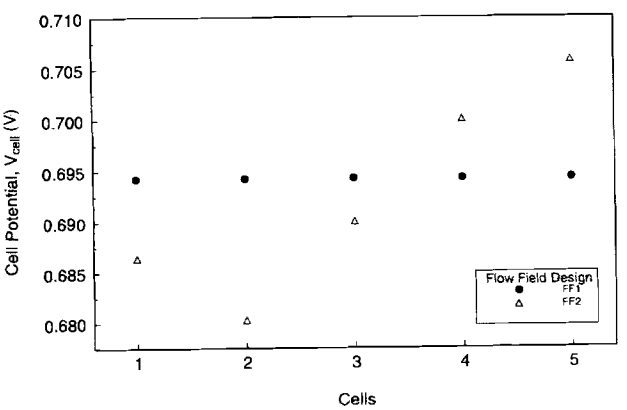

Fig. 13. Variation of cell voltages across the fuel-cell stack. Effect of flow-field design.

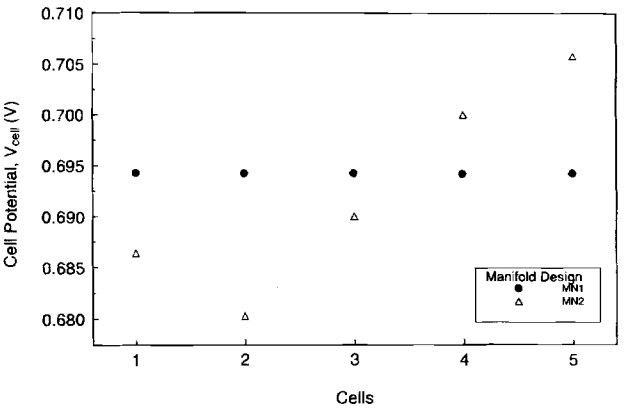

Fig. 14. Variation of cell voltage across the stack. Effect of anode-manifold dimensions.

$$\text{Power} = I \sum_{j=1}^{N} V_j \qquad [15]$$

The results are 208.26 W with flow-field design FF1 and 207.75 W with design FF2. Hence it can be inferred that nonuniformity in the cell performance leads to a decrease in the power generated.

The effect of the gas-manifold dimensions can be determined from Fig. 14. It is seen that a smaller manifold dimension, design MN2, leads to nonuniformity in the gas distribution and hence may result in inefficient stack operation. A smaller manifold is usually preferred as it increases the volumetric efficiency of the fuel-cell stack and minimizes problems associated with sealing.

Conclusion

The result of the sensitivity analysis with the single-cell model identified the inlet flow rate of the reactant gases as one of the important parameters affecting the operation of a fuel cell at fixed current density. The performance of the fuel-cell stack is modeled as a function of the various interacting subsystems. The gas distribution and hence the stack operating efficiency are found to be very much dependent on the flow-field design used. The existence of an optimal flow field and manifold design in the context of the fuel-cell power system is identified. The advantage of modular construction of the stack model is fully realized as the effect of different flow-field and manifold designs on the stack performance can be easily tested.

Acknowledgment

The authors are grateful for the support of this work by the DOE/EPSCoR program, Cooperative Agreement No. DE-FC02-91ER75666.

Manuscript submitted June 3, 1996; revised manuscript received Dec. 1, 1996.

The University of South Carolina assisted in meeting the publication costs of this article.

LIST OF SYMBOLS

a	half-width of the rectangular duct forming the grooves/channels in the flow field, cm
b	half-height of the rectangular duct forming the grooves/channels in the flow field, cm
$ffi(n)$	inlet flow rate of the gas into the nth fuel cell in the stack, (cm^3/s)
$ffo(n)$	inlet flow rate of the gas into the nth fuel cell in the stack, (cm^3/s)
h	pressure of the gas (Pa)
I_{avg}	average operating current density of the fuel cell, A/cm^2

Downloaded on 2014-10-20 to IP 129.252.69.176 address. Redistribution subject to ECS terms of use (see ecsdl.org/site/terms_use) unless CC License in place (see abstract).

$I(x)$ local current density, A/cm^2
$k1$, $k2$ conductance for the gas flow in the grooves/channels of the flow field, cm^3/Pa s
ki, ko conductance for the gas flow in the manifold, cm^3/Pa s
k discharge or entrance coefficient for the gas flow in the manifold
L length of the fuel cell, in the direction of gas flow, cm
nh number of channels in the flow field perpendicular to the general direction of gas flow
nv number of channels in the flow field parallel to the general direction of gas flow (grooves)
$p1(n)$ pressure in the inlet manifold at the upstream end of the branch at the nth cell, Pa
$p1d(n)$ pressure in the inlet manifold at the downstream end of the branch at the nth cell, Pa
$p2(n)$ pressure in the outlet manifold at the upstream end of the branch at the nth cell, Pa
$p2d(n)$ pressure in the outlet manifold at the downstream end of the branch at the nth cell, Pa
Q consumption of the reactant, cm^3/s
q flow rate of the gas, cm^3/s
S_p^V sensitivity of the cell voltage with respect to the parameter, p (V)
$u1$ velocity of the gas flow in the inlet manifold, cm/s
$u2$ velocity of gas flow in the outlet manifold, cm/s
U reactant utilization
V cell voltage, V
x distance along the length of the cell from the inlet, cm

Subscripts
D outlet end of the flow field
E entrance region of the flow field
i species i (H_2, O_2, or H_2O)
i, j node, i, j in the rectilinear groove network in the flow field

Greek
μ viscosity of the gas, Pa s
ρ density of the gas, kg/cm^3
ΔP pressure difference between the inlet and outlet of the rectangular flow channel, Pa
Δx length of the rectangular flow channel, cm

REFERENCES

1. T. V. Nguyen and R. E. White, *This Journal*, **140**, 2178 (1993).
2. T. F. Fuller and J. Newman, *ibid.*, **140**, 1218 (1993).
3. D. M. Bernardi and M. W. Verbrugge, *AIChE. J.*, **37**, 1151 (1991).
4. J. C. Amphlett, R. M. Baumert, R. F. Mann, B. A. Peppley, and P. R. Roberg, *This Journal*, **142**, 9 (1995).
5. M. Caracotsios and W. E. Stewart, *Comput. Chem., Eng.*, **9**, 359 (1985).
6. F. M. White, *Viscous Fluid Flow*, p. 120, McGraw-Hill, Inc., New York (1991).
7. *User's Manual*, MATH/LIBRARY-Vol 1, IMSL, Inc. (1991).
8. R. L. Pigford, M. Ashraf, and Y. D. Miron, *Ind. Eng. Chem. Fundam.*, **22**, 463 (1983).
9. J. Morè, B. Garbow, and K. Hillstrom, *User's Guide for MINPACK-1*, ANL- 80-74, Argonne National Labs Report, Argonne, IL (1980).

Mott-Schottky Analysis of Nanometer-Scale Thin-Film Anatase TiO_2

R. van de Krol, A. Goossens,* and J. Schoonman*

Laboratory for Applied Inorganic Chemistry, Delft University of Technology, 2628 BL Delft, The Netherlands

ABSTRACT

Smooth nanometer-scale films of anatase TiO_2 on indium-tin oxide substrates (ITO) are obtained by electron-beam evaporation of reduced TiO_2 powder. Mott-Schottky analysis shows an abrupt change in slope when the depletion layer reaches the TiO_2/ITO interface. An electrostatic model is derived, which gives a quantitative description of the observed change in slope. From the potential at which the slope changes, the dielectric constant of anatase could be accurately determined. A value of 55 is found, which is significantly lower than those reported for anatase TiO_2.

Introduction

Recently, much attention has been focused on the use of nanostructured metal oxide semiconductors for various applications, such as electrochromic windows,[1] photocatalytic devices,[2] lithium-ion batteries,[3] dielectrics in integrated circuits,[4] and dye-sensitized TiO_2 solar cells.[5] In porous nanostructured films, the fraction of atoms located at or near the surface is very large. For example, in spherical anatase TiO_2 particles with a diameter of 5 nm, approximately 7% of the atoms is located at the surface, and an even larger fraction of the atoms is in proximity to it and experiences an anisotropic environment. This has a significant effect on the electronic structure, as well as on the related opto-electronic properties of porous nanostructured semiconductors. Due to the large specific surface area, there is an accompanying large number of chemical reaction and/or adsorption sites present. This feature is used in dye-sensitized TiO_2 solar cells, in which the nanoporous structure allows a huge increase in the number of adsorbed dye-molecules (compared to flat surfaces), thereby greatly enhancing the efficiency of the device.[5]

Improving existing devices based on porous nanostructured TiO_2, and developing new ones, requires detailed understanding of the fundamental properties of (nanostructured) anatase TiO_2. Although a vast number of studies has already been dedicated to porous nanostructured metal oxides, especially anatase TiO_2, many fundamental questions remain unanswered.[6] Some work has been done on single crystals to get a better understanding of the bulk properties of anatase TiO_2.[7-9] However, these crystals are reported to have a large number of defects and in some cases a high aluminium impurity content,[7] resulting in donor densities of the order of 10^{19} cm^{-3}, while porous nanostructured electrodes have donor densities of the order of 10^{17} cm^{-3}.[10,11] Since the donor density is expected to have a significant influence on various (opto-)electronic properties, the reported bulk properties for anatase single crystals may differ from those of porous nanostructured electrodes.

To overcome the complexities which are introduced by the porous topology while keeping the donor density comparable to that of porous films, very thin smooth films of TiO_2 are investigated here. These films possess a simple geometry while having a relatively high surface-to-volume ratio. They also have a comparable donor density, as will

* Electrochemical Society Active Member.

Downloaded on 2014-10-20 to IP 129.252.69.176 address. Redistribution subject to ECS terms of use (see ecsdl.org/site/terms_use) unless CC License in place (see abstract).